Electronic Supplementary Material (ESI) for Dalton Transactions.

Modulating nickel-iron active species via dealloying for boosting oxygen evolution reaction

Zhuqing Wan[a], Xiaolong Guo[a*], Junying Jiang[a], Yuci Xin[a], Benzhen Tang[a],

Hong Zhang[a], Yong Wu[a,b*], Lei Xia[b], Peng Yu[a,*]

[a] College of Physics and Electronic Engineering of Chongqing Normal University, Chongqing Key Laboratory of Optical and Electronic Functional Materials, Chongqing 401331, China

[b] Institute of Materials & Laboratory for Microstructure, Shanghai University, Shanghai 200072, China

[*]Corresponding author.

Email address: guoxiaolong@cqnu.edu.cn (X. Guo), wy_yp@shu.edu.cn (Y. Wu),

pengyu@cqnu.edu.cn (P. Yu)

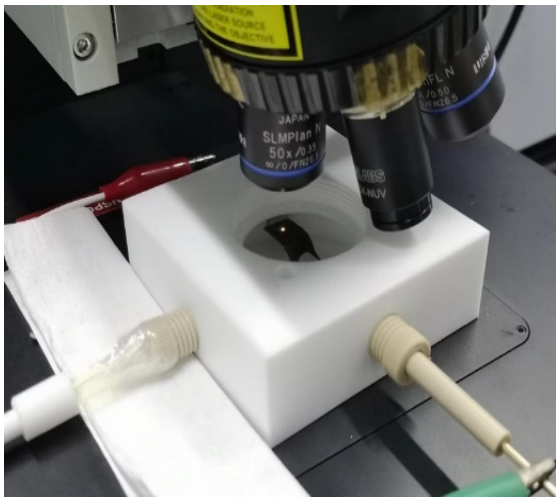

Fig.S1. The optical photos of the Raman spectrometer.

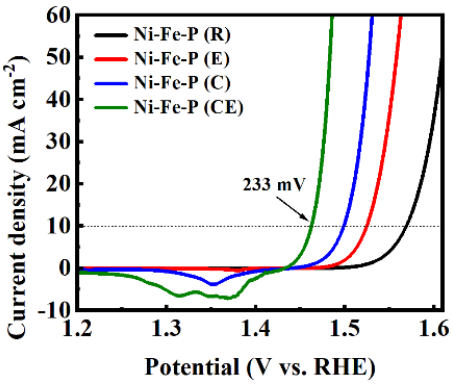

Fig. S2 LSV curves of the Ni-Fe-P ribbons. Note: LSV curves are scanned from high voltage to low voltage.

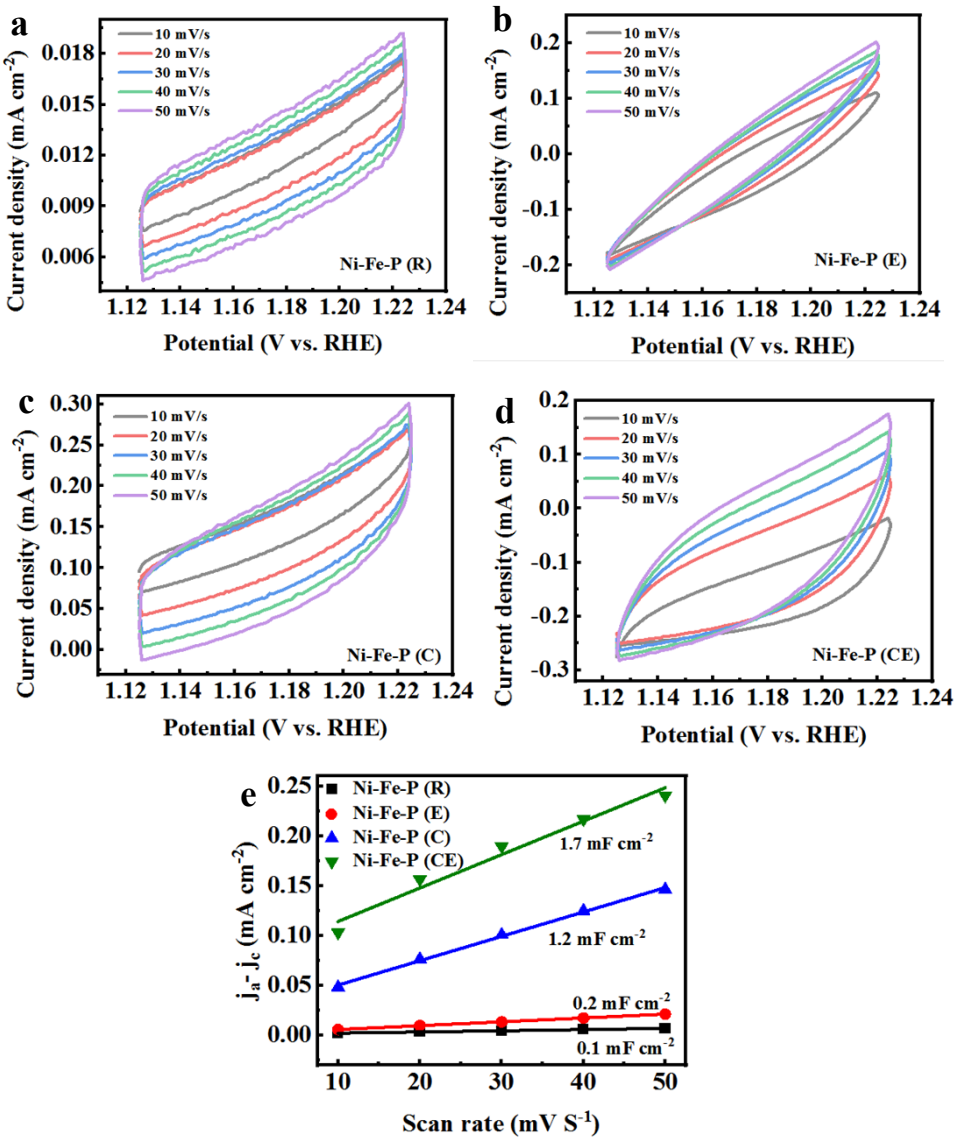
a
10 mV/s
20 mV/s
30 mV/s
40 mV/s
50 mV/s
Ni-Fe-P (R)
Current density (mA cm-2)
Potential (V vs. RHE)
b
Ni-Fe-P (E)
c
Ni-Fe-P (C)
d
Ni-Fe-P (CE)
e
Ni-Fe-P (R)
Ni-Fe-P (E)
Ni-Fe-P (C)
Ni-Fe-P (CE)
1.7 mF cm-2
1.2 mF cm-2
0.2 mF cm-2
0.1 mF cm-2
ja- jc (mA cm-2)
Scan rate (mV S-1)

Fig. S3 (a-d)

Cyclic voltammograms at E =1.125–1.225 V vs. RHE and (e) scan rate dependence of the current density at E = 1.18 V vs. RHE for assessing the double layer capacitance.

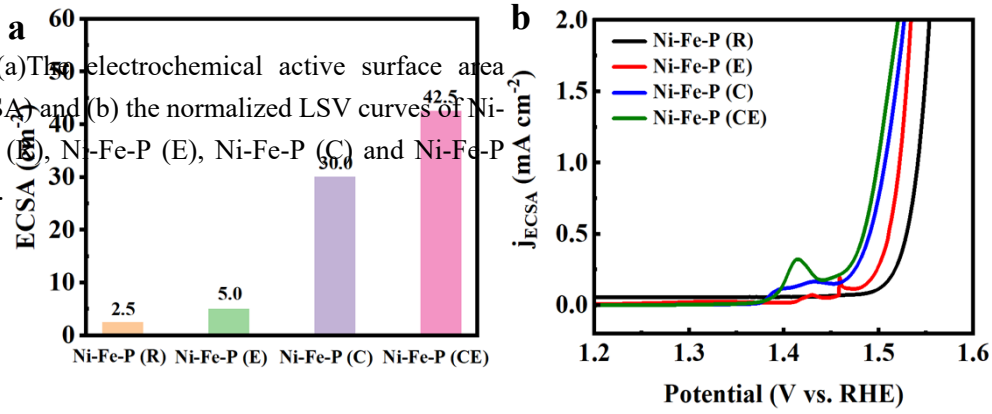

Fig. S4. (a)The electrochemical active surface area (ECSA) and (b) the normalized LSV curves of Ni-Fe-P (R), Ni-Fe-P (E), Ni-Fe-P (C) and Ni-Fe-P (CE).

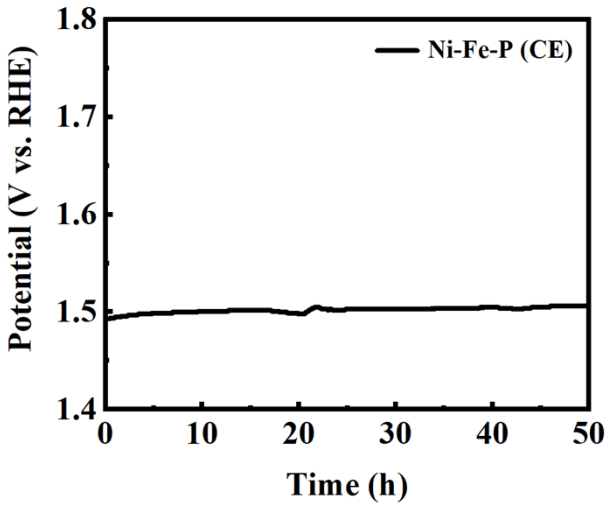

Fig. S5 The stability test of Ni-Fe-P (CE) at 10 mA cm^{-2} for 50 hours.

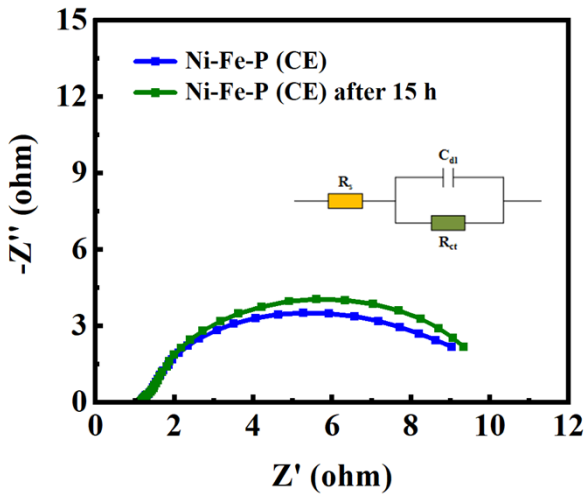

Fig. S6. Electrochemical impedance spectroscopy (EIS) of Ni-Fe-P (CE) before and after stability test.

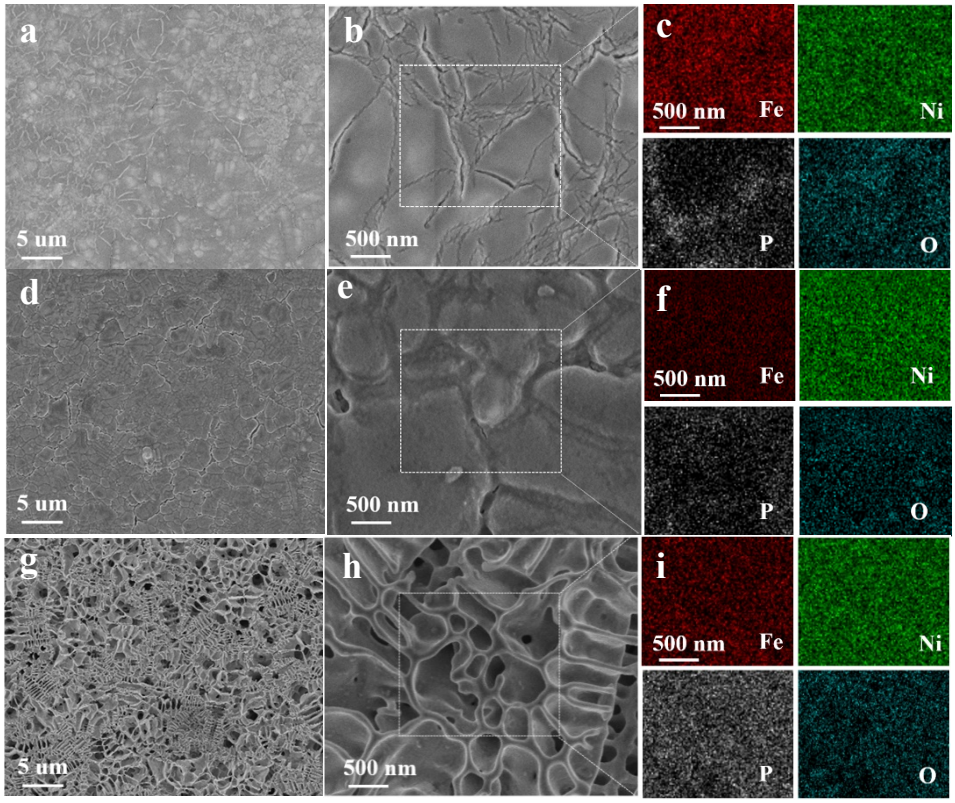

Fig. S7. SEM images and EDS mapping of (a-c) Ni-Fe-P (R) , (d-f) Ni-Fe-P (C) and (g-i) Ni-Fe-P (E) after the stability tests (15 h).

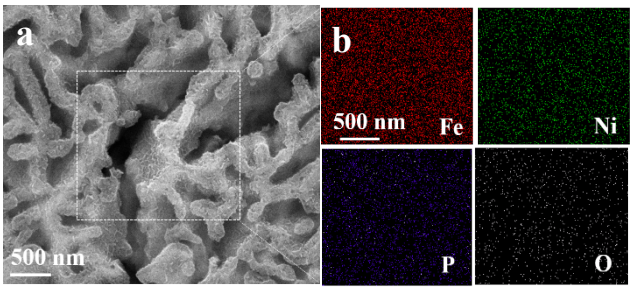

Fig. S8. SEM images and EDS mapping of Ni-Fe-P (CE) after the stability tests (15 h).

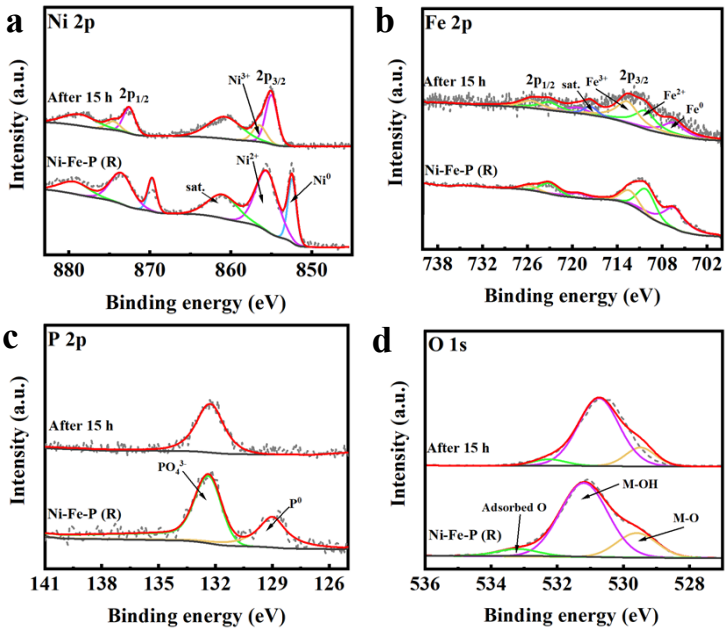

Fig. S9 XPS spectra of Ni-Fe-P (R) before and after the stability test (15 h): (a) Ni 2p, (b) Fe 2p, (c) P 2p, and (d) O 1s.

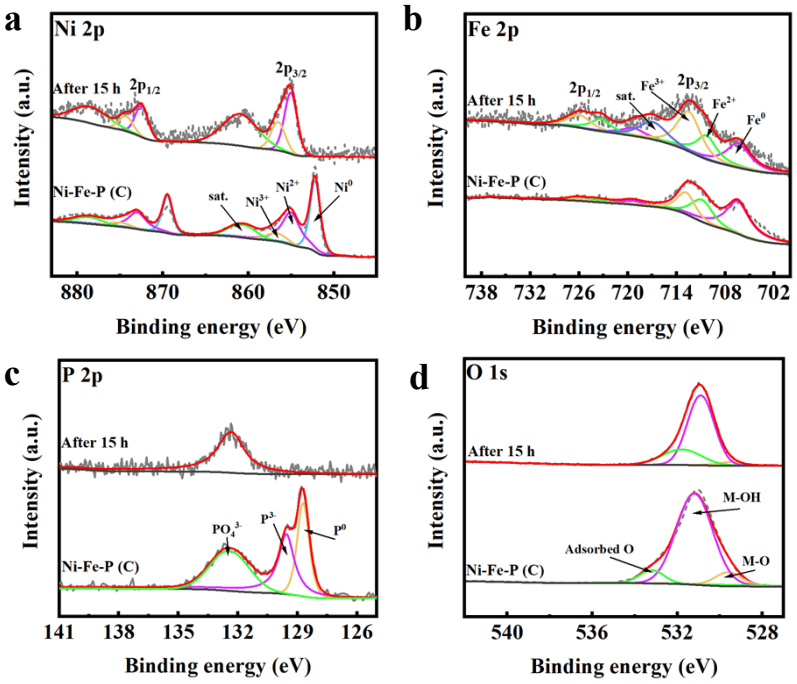

Fig. S10. XPS spectra of Ni-Fe-P (C) before and after the stability test (15 h): (a) Ni 2p, (b) Fe 2p, (c) P 2p, and (d) O 1s.

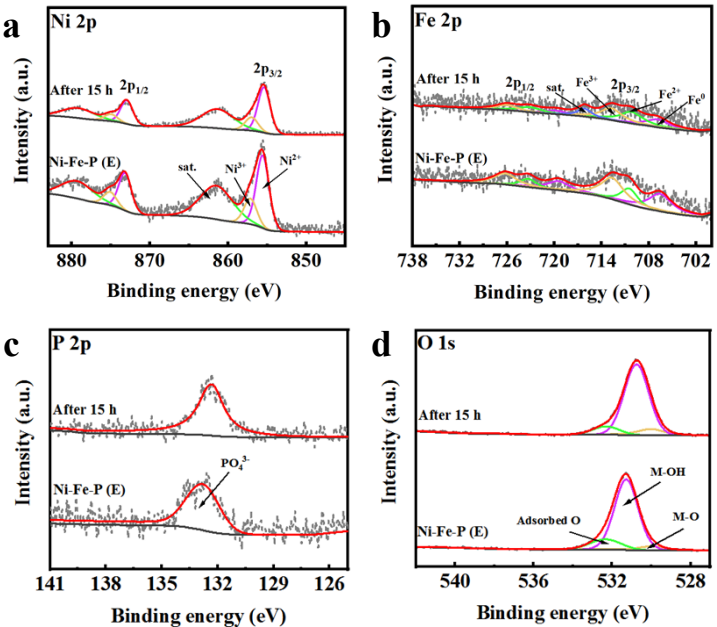

Fig. S11. XPS spectra of Ni-Fe-P (E) before and after the stability test (15 h): (a) Ni 2p, (b) Fe 2p, (c) P 2p, and (d) O 1s.

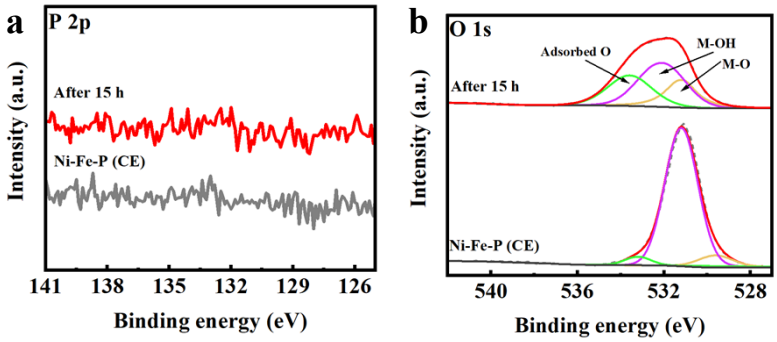

Fig. S12. XPS spectra of Ni-Fe-P (CE) before and after stability test: (c) P and (d) O.

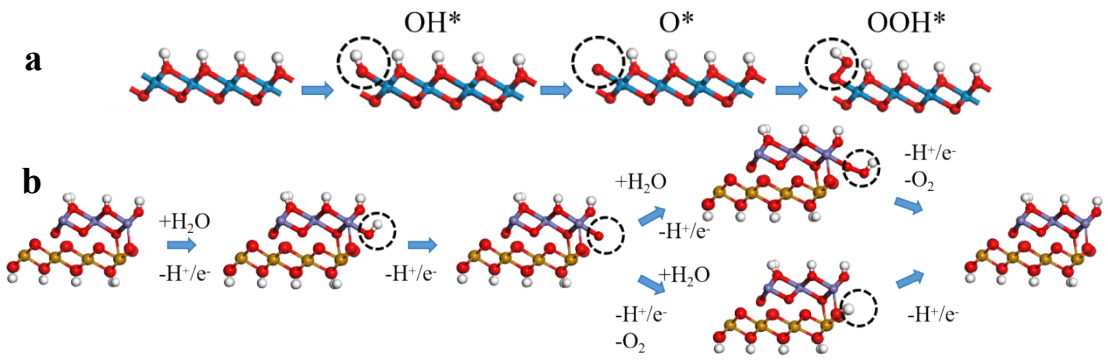

Fig. S13. (a) Standard orientation of the NiOOH model and the adsorbed OH*, O* and OOH* intermediates on the Ni sites of NiOOH model. (b) Standard orientation of the NiOOH/FeOOH model and the adsorbed OH*, O* and OOH* intermediates on the Fe-Ni dual sites of NiOOH/ FeOOH model. Brown balls: Fe atoms; Blue balls: Ni atoms; Red balls: O atoms; White balls: H atoms.

For OER catalyzed by metal oxyhydroxides, the commonly mechanism involves four consecutive proton-coupled electron transfer (PCET), where the adsorption of OH*, O*, and OOH* is successively on the one site [1]. The mechanism diagram is shown in **Fig. S13a**, which is suitable for the monospecies NiOOH derived by Ni-Fe-P (R). The OER mechanism of the NiOOH/FeOOH species (Ni-Fe-P (CE)) is bifunctional mechanism [2]. This mechanism involves two catalytic sites, often based on two different metal ions, which work in a cooperative manner (**Fig. S**13b). One site (such as, Fe sites) provides the electrophilic M=O entity, while the other side (such as, Ni sites) provides a hydrogen atom acceptor.

Table S1. The content of Ni, Fe, P, and O on the surface and cross-section of Ni-Fe-P (CE).

	Surface	Cross-section
Ni (at.%)	42.3	50.2
Fe (at.%)	9.0	21.7
P (at.%)	7.1	5.5
O (at.%)	41.5	22.6

Table S2. The peak positions of the various ions in the XPS results.

	Fe^0 (eV)	Fe^{2+} (eV)	Fe^{3+} (eV)	Ni^0 (eV)	Ni^{2+} (eV)	Ni^{3+} (eV)	PO_4^{3-} (eV)	P^{3-} (eV)	P^0 (eV)
Ni-Fe-P (R)	706.5	710.1	712.8	852.5	855.4	\	132.8	\	128.9
Ni-Fe-P (E)	706.3	710.5	712.7	852.3	855.0	856.6	132.5	\	128.8
Ni-Fe-P (C)	706.6	710.9	712.8	\	855.7	857.1	132.4	129.5	128.8
Ni-Fe-P (CE)	706.6	710.5	712.9	\	855.6	856.7	\	\	\

Table S3 Comparison of OER performance with recently reported ribbons and other oxide electrocatalysts in alkaline media.

Catalysts	Overpotentials (mV)	References
Dealloyed Ni-Fe-P ribbon	234 mV@10 mA cm^{-2}	This work
$Na_2Co_{0.75}Fe_{0.25}P_2O_7$/C NPs	300 mV@10 mA cm^{-2}	[3]
DR-NiOOH	281 mV@10 mA cm^{-2}	[4]
CR-NiOOH	278 mV@10 mA cm^{-2}	[5]
α-Fe_2O_3	317 mV@10 mA cm^{-2}	[6]
Glassy $Ni_{40}Fe_{40}P_{20}$	270 mV@10 mA cm^{-2}	[7]
np-NiFeP	287 mV@10 mA cm^{-2}	[8]
Acid treated NiFeP	219 mV@10 mA cm^{-2}	[9]
glassy FeNiCoP	281 mV@10 mA cm^{-2}	[10]
$Fe_{40}Ni_{20}Co_{20}P_{15}C_5$	278 mV@10 mA cm^{-2}	[11]
$(Ni_{0.67}Fe_{0.33})_4P_5$	245 mV@10 mA cm^{-2}	[12]
Treated FeNiPC	289 mV@10 mA cm^{-2}	[13]
$Ni_{59}Cu_{19}P_9$	307 mV@10 mA cm^{-2}	[14]
nanocages FeNiPBO	236 mV@10 mA cm^{-2}	[15]
CoFeP NFs/NPCNT	278 mV@10 mA cm^{-2}	[16]
FeP_4 cubes	283 mV@10 mA cm^{-2}	[17]
Fe-Co-P	269 mV@10 mA cm^{-2}	[18]
$FeNi(VO_4)_x$@NF	274 mV@10 mA cm^{-2}	[19]
$Ni_{0.8}Co_{0.1}Fe_{0.1}O_xH_y$	239 mV@10 mA cm^{-2}	[20]
$Ni_{40}Fe_{40}B_{20}$	319 mV@10 mA cm^{-2}	[21]
$Ni_{14}Co_{14}Fe_{14}Mo_6Mn_{52}$	350 mV@10 mA cm^{-2}	[22]
$Fe_{50}Ni_{30}P_{13}C_7$	289 mV@10 mA cm^{-2}	[23]
np-$(Ni_{0.75}Fe_{0.25})_4P_5$	280 mV@10 mA cm^{-2}	[24]
$(Ni_{0.4}Fe_{0.4}B_{0.2})_{100-x}Ru_x$ (x=0)	295 mV@10 mA cm^{-2}	[25]
$Ni_{40}Fe_{20}Co_{20}P_{20}$	244 mV@10 mA cm^{-2}	[26]

$Fe_{35}Co_{20}Ni_{20}Mo_{20}Si_5$	260 mV@10 mA cm^{-2}	[27]

Table S4 Charge-transfer resistance (R_{ct}) of the ribbons in the electrochemical impedance spectroscopy (EIS).

Sample	R_s	R_{ct} (ohm)
Ni-Fe-P (R)	1.339	2250
Ni-Fe-P (E)	1.285	525.7
Ni-Fe-P (C)	1.473	17.1
Ni-Fe-P (CE)	1.173	8.99

Table S5 The parameters of the electrochemical impedance spectroscopy (EIS) before and after stability test. Note: R_s is the solution resistance (small arc in front), R_{ct} is the interface resistance (circular arc in the back), and the magnitude of R_p can reflect the corrosion rate. The capacitance CPE-T is a double-layer capacitance, and CPE-P is the dispersion index.

Sample	R_s	R_{ct} (ohm)	CPE-T	CPE-P
Ni-Fe-P (CE)	1.173	8.99	0.4366	0.85
Ni-Fe-P (CE) after stability test	1.177	9.94	0.3990	0.85

Table S6 The ratios of Ni and Fe ions for Ni-Fe-P (R), Ni-Fe-P (C), Ni-Fe-P (E) and Ni-Fe-P (CE).

		Ni-Fe-P (R)	Ni-Fe-P (C)	Ni-Fe-P (E)	Ni-Fe-P (CE)	Ni-Fe-P (R) After 15 h	Ni-Fe-P (C) After 15 h	Ni-Fe-P (E) After 15 h	Ni-Fe-P (CE) After 15 h
	Fe^0	53.29	57.26	28.90	28.63	24.02	29.9	24.64	27.1
Fe	Fe^{2+}	4.41	11.65	44.36	29.02	34.28	26.0	38.23	30.58
(at.%)	Fe^{3+}	42.3	31.1	26.62	42.35	41.7	44.15	37.12	42.34
	Ni^0	27.3	49.8	0	0	0	0	0	0
Ni	Ni^{2+}	72.7	41.9	73.4	58.4	72.26	75.22	64.84	46.3
(at.%)	Ni^{3+}	0	8.3	26.6	41.6	27.74	24.78	35.16	53.7

Table S7. The values of δ (Ni-O)/Ni-O and Fe-O/Ni-O under different potentials vs. Ag/AgCl in in-situ Raman test for Ni-Fe-P (R).

	δ (Ni-O)/Ni-O	Fe-O/Ni-O
0.30 V	0	0
0.35 V	0	0
0.40 V	0	0
0.45 V	0	0
0.50 V	0.68	0
0.55 V	0.55	0
0.60 V	0.72	0

Table S8. The value of δ (Ni-O)/Ni-O and Fe-O/Ni-O under different potentials vs. Ag/AgCl in in-situ Raman test for Ni-Fe-P (C).

	δ (Ni-O)/Ni-O	Fe-O/Ni-O
0.30 V	0	0.27
0.35 V	0	0.12
0.40 V	0	0.18
0.45 V	0	0.34
0.50 V	0.74	0
0.55 V	0.69	0
0.60 V	0.70	0.05

Table S9. The value of δ (Ni-O)/Ni-O and Fe-O/Ni-O under different potentials vs.Ag/AgCl in in-situ Raman test for Ni-Fe-P (CE).

	δ (Ni-O)/Ni-O	Fe-O/Ni-O
0.30 V	0	0.14
0.35 V	0	0.21
0.40 V	0	0.12
0.45 V	0	0.17
0.50 V	0	0.19
0.55 V	0	0.25
0.60 V	0	0.21

References

[1] I. C. Man, H.-Y. Su, F. Calle-Vallejo, H. A. Hansen, J. I. Mart&nez, N. G. Inoglu, J. Kitchin, T. F. Jaramillo, J. K. Nørskov,J. Rossmeisl, Universality in Oxygen Evolution Electrocatalysis on Oxide Surfaces, ChemCatChem 2011, 3, 1159-1165.

[2] L. C. Bai, Dr. S. Lee,X. L. Hu, Spectroscopic and Electrokinetic Evidence for a Bifunctional Mechanism of the Oxygen Evolution Reaction; An Unconventional Iron Nickel Catalyst for the Oxygen Evolution Reaction, Angew. Chem. Int. Ed., 2021, 6, 3095-3103.

[3] H. J. Song, H. Yoon, B. Ju, D. Y. Lee, D. W. Kim, Electrocatalytic Selective Oxygen Evolution of Carbon-Coated $Na_2Co_{1-x}FexP_2O_7$ Nanoparticles for Alkaline Seawater Electrolysis, ACS Catal., 2020, 10, 702-709.

[4] X. Liu, K. Ni, B. Wen, R. Guo, C. Niu, J. Meng, Q. Li, P. Wu, Y. Zhu, X. Wu, L. Mai, Deep Reconstruction of Nickel-Based Precatalysts for Water Oxidation Catalysis, ACS Energy Lett., 2019, 4, 2585-2592.

[5] X. Liu, J. Meng, K. Ni, R. Guo, F. Xia, J. Xie, X. Li, B. Wen, P. Wu, M. Li, J. Wu, X. Wu, L. Mai, D. Zhao, Complete Reconstruction of Hydrate Pre-Catalysts for Ultrastable Water Electrolysis in Industrial-Concentration Alkali Media, Cell Reports Phys. Sci., 2020, 1, 100241.

[6] H. Wu, T. Yang, Y. H Du, L. Shen, G. W. Ho, Identification of Facet-Governing Reactivity in Hematite for Oxygen Evolution, Adv. Mater., 2018,30, 1804341.

[7] Y. Tan, F. Zhu, H. Wang, Y. Tian, A. Hirata, T. Fujita, M. Chen, Noble-Metal-Free Metallic Glass as a Highly Active and Stable Bifunctional Electrocatalyst for Water Splitting, Adv. Mater. Interfaces, 2017,4, 1601086.

[8] Y. Pang, W. Xu, S. Zhu, Z. Cui, Y. Liang, Z. Li, S. Wu, C. Chang, S. Luo, Self-supporting amorphous nanoporous NiFeCoP electrocatalyst for efficient overall water splitting, J. Mater. Sci. Technol., 2021, 82, 96-104.

[9] F. Hu, S. Zhu, S. Chen, Y. Li, L. Ma, T. Wu, Y. Zhang, C. Wang, C. Liu, X. Yang, L. Song, X. Yang, Y. Xiong, Amorphous Metallic NiFeP: A Conductive Bulk Material Achieving High Activity for Oxygen Evolution Reaction in Both Alkaline and Acidic Media, Adv. Mater., 2017, 29, 1606570.

[10] S. Jiang, L. Zhu, Z. Yang, Y. Wang, Enhanced electrocatalytic performance of FeNiCoP amorphous alloys as oxygen-evolving catalysts for electrolytic water splitting application, Electrochim. Acta, 2021, 368, 137618.

[11] K. S. Aneeshkumar, J. Tseng, X. Liu, J. Tian, D. Diao, J. Shen, Electrochemically dealloyed nanoporous $Fe_{40}Ni_{20}Co_{20}P_{15}C_5$ metallic glass for efficient and stable electrocatalytic hydrogen and oxygen generation, RSC Adv., 2021,11, 7369-7380.

[12] W. Xu, S. Zhu, Y. Liang, Z. Cui, X. Yang, A nanoporous metal phosphide catalyst for bifunctional water splitting, J. Mater. Chem. A, 2018,6, 5574-5579.

[13] Z. Jia, Y. Zhao, Q. Wang, F. Lyu, X. Tian, S. Liang, L. Zhang, J. Luan, Q. Wang, L. Sun, T. Yang, B. Shen, Nanoscale Heterogeneities of Non-Noble Iron-Based Metallic Glasses toward Efficient Water Oxidation at Industrial-Level Current Densities, ACS Appl. Mater. Interfaces, 2022, 14, 10288-10297.

[14] B. K. Kim, S. Kim, S. K. Cho, J. J. Kim, Enhanced catalytic activity of electrodeposited Ni-Cu-P toward oxygen evolution reaction, Appl. Catal. B: Environ., 2018, 237, 409-415.

[15] H. Ren, X. Sun, C. Du, J. Zhao, D. Liu, W. Fang, S. Kumar, R. Chua, S. Meng, P. Kidkhunthod, L. Song, S. Li, S. Madhavi, Q. Yan, Amorphous Fe-Ni-P-B-O nanocages as efficient electrocatalysts for oxygen evolution reaction, ACS Nano, 2019, 13, 12969–12979.

[16] W. Li, Y. Chen, B. Yu, Y. Hu, X. Wang, D. Yang, 3D hollow Co–Fe–P nanoframes immobilized on N, P-doped CNT as an efficient electrocatalyst for overall water splitting, Nanoscale, 2019, 11, 17031-17040.

[17] Q. He, H. Xie, Z.u. Rehman, C. Wang, P. Wan, H. Jiang, W. Chu, L. Song, Highly Defective Fe-Based Oxyhydroxides from Electrochemical Reconstruction for Efficient Oxygen Evolution Catalysis, ACS Energy Lett., 2018, 3, 861-868.

[18] H. Zhang, W. Zhou, J. Dong, X.F. Lu, X.W. Lou, Intramolecular electronic coupling in porous iron cobalt (oxy)phosphide nanoboxes enhances the electrocatalytic activity for oxygen evolution, Energy Environ. Sci., 2019, 12, 3348-3355.

[19] K. Dastafkan, Q. Meyer, X. Chen, C. Zhao, Efficient Oxygen Evolution and Gas Bubble Release Achieved by a Low Gas Bubble Adhesive Iron–Nickel Vanadate Electrocatalyst, Small, 2020, 16, 2002412.

[20] Q. Zhao, J. Yang, M. Liu, R. Wang, G. Zhang, H. Wang, H. Tang, C. Liu, Z. Mei, H. Chen, F. Pan, Tuning Electronic Push/Pull of Ni-Based Hydroxides To Enhance Hydrogen and Oxygen Evolution Reactions for Water Splitting , ACS Catal., 2018, 8, 5621-5629.

[21] H.-L. Li, Y. -Y. Wang, C.-M. Liu, S.-M. Zhang, H.-F. Zhang, Z.-W. Zhu, Enhanced OER performance of NiFeB amorphous alloys by surface self-reconstruction, Int. J. Hydrog. Energy, 2022, 47, 20718-20728.

[22] H. Liu, H. Y. Qin, J. L. Kang, L. Y. Ma, G. X. Chen, Q. Huang, Z. J. Zhang, E. Z. Liu, H. M. Lu, J. X. Li, N. Q. Zhao, A freestanding nanoporous NiCoFeMoMn high-entropy alloy as an efficient electrocatalyst for rapid water splitting, Chem. Eng. J., 2022, 435, 134898.

[23] Z. Jia, Y. L. Zhao, Q. Wang, F. C. Lyu, X. B. Tian, S.-X. Liang, L.-C. Zhang, J. H. Luan, Q. Q. Wang, L. G. Sun, T. Yang, B. L. Shen, Nanoscale heterogeneities of non-noble iron-based metallic glasses toward efficient water oxidation at industrial-level current densities, ACS Appl. Mater. Interfaces, 2022, 14, 10288–10297.

[24] W. Xu, S. L. Zhu, Y. Q. Liang, Z. D. Cui, X. J. Yang, A. Inoue, A nanoporous metal phosphide catalyst for bifunctional water splitting, J. Mater. Chem. A, 2018, 6, 5574-5579.

[25] G. G. Xi, L. Zuo, X. Li, Y. Jin, R. Li, T. Zhang, In-situ constructed Ru-rich porous framework on NiFe-based ribbon for enhanced oxygen evolution reaction in alkaline solution, J. Mater. Sci. Technol., 2021, 70, 197-204.

[26] Y. Pang, W. Xu, S. L. Zhu, Z. D. Cui, Y. Q. Liang, Z. Y. Li, S. L. Wu, C. Chang, S. Y. Luo, Self-supporting amorphous nanoporous NiFeCoP electrocatalyst for efficient overall water splitting, J. Mater. Sci. Technol., 2021, 82, 96-104.

[27] Y. Wu, Q. X. Chen, Q. Zhang, C. Bai, J. X. Peng, B. Z. Tang, D. M. Li, D. Ding, L. Xia, X. L. Guo, P. Yu, Self-supported electrode $Fe_{35}Co_{20}Ni_{20}Mo_{20}Si_5$ alloy ribbon: Electronic structure modulating oxygen evolution reaction, J. Alloys Compd., 2022, 911, 164993.